APS physics

CHORUS

This is the accepted manuscript made available via CHORUS. The article has been published as:

Evidence of Mott physics in iron pnictides from x-ray spectroscopy

S. Lafuerza, H. Gretarsson, F. Hardy, T. Wolf, C. Meingast, G. Giovannetti, M. Capone, A. S. Sefat, Y.-J. Kim, P. Glatzel, and L. de' Medici

Phys. Rev. B **96**, 045133 — Published 24 July 2017

DOI: 10.1103/PhysRevB.96.045133

Evidences of Mott physics in iron pnictides from x-ray spectroscopy

S. Lafuerza[1,*], H. Gretarsson[2], F. Hardy[3], T. Wolf[3], C. Meingast[3], G. Giovannetti[4], M. Capone[4], A. S. Sefat[5], Y. –J. Kim[6], P. Glatzel[1,*] and L. de' Medici[1,*]

[1]*ESRF – The European Synchrotron, CS40220, F-38043 Grenoble Cedex 9, France*
[2]*Max-Planck-Institut für Festkörperforschung, Heisenbergstraße 1, D-70569 Stuttgart, Germany*
[3]*Karlsruher Institut für Technologie, Institut für Festkörperphysik, 76021 Karlsruhe, Germany*
[4]*CNR-IOM-Democritos National Simulation Centre and International School for Advanced Studies (SISSA), Via Bonomea 265, I-34136, Trieste, Italy*
[5]*Materials Science and Technology Division, Oak Ridge National Laboratory, Oak Ridge, Tennessee 37831-6114, USA*
[6]*Department of Physics, University of Toronto, 60 St. George St., Toronto, Ontario, M5S 1A7, Canada*
*E-mail: sara.lafuerza@esrf.fr, demedici@esrf.fr, pieter.glatzel@esrf.fr

Abstract

The existence of large instantaneous local magnetic moments in paramagnetic phases is a direct signature of Mott localization. In order to track the doping evolution of fluctuating local moments in iron-based superconductors, we jointly use two fast probes, x-ray emission and absorption spectroscopy. Exploring K- and Cr- hole-doped $BaFe_2As_2$ we find a systematic increase in the local moment with hole-doping, in contrast with inelastic neutron scattering measurements which suggest an opposite trend. Our results support the theoretical scenario in which a Mott insulating state that would be realized for half-filled conduction bands has an influence throughout the phase diagram of these iron pnictides.

I. INTRODUCTION

The role of electron-electron correlations in the iron-based superconductors remains elusive, with seemingly contradictory evidences suggesting either a weakly-correlated or a strongly-correlated picture for the conduction electrons in orbitals which have Fe-3*d* character. A scenario has recently been proposed, where the dichotomy is resolved and the low energy physics is described in terms of a coexistence of strongly and weakly correlated electrons [1]. Such a picture provides a framework to understand a wealth of experiments on quasiparticle mass enhancements (specific heat, low-frequency optical conductivity, angle-resolved photoemission spectroscopy, quantum oscillations etc.) in electron- and hole-doped $BaFe_2As_2$ [1–3]. A central aspect of the proposal is that the degree of correlation is controlled by the distance in doping from a Mott-insulating state favoured by Hund's coupling that would be realized if the system could be doped until the d^5 configuration (half-filling of the five Fe-3*d* conduction bands). The influence of this putative Mott insulator extends in the actual range of doping in which these materials exist, from $d^{5.5}$ (for hole-doped compounds, like KFe_2As_2) to d^6 (for the stoichiometric parent compound $BaFe_2As_2$) and beyond (for electron-doped compounds). Indeed in doped $BaFe_2As_2$ the quasiparticle masses increase continuously from the electron-doped to the hole-doped side of the phase diagram, and in the same process, a strong differentiation between the effective masses in different orbitals develops [4].

If this scenario is correct, the electronic correlations associated with the proximity to the Mott insulator should also lead to large local moments in the paramagnetic phase above any magnetic or superconducting ordering. The Hund's coupling-driven Mott insulator with 5 electrons in 5 orbitals would be in the high-spin state (S = 5/2) [5,6] and the neighbouring metallic phase is also expected to be dominated by high-spin configurations. Therefore, starting from the d^6 parent compound, one would expect a build-up of the magnetic moment with hole-doping towards this saturated value. An experimental confirmation of this high-energy counterpart of the aforementioned quasiparticle behaviour would highlight the role of Mott physics in these materials. A direct proof of this scenario requires a fast local probe in order to capture rapidly fluctuating moments in a paramagnetic metal. We thus use here *Kβ* core-to-core (CTC) x-ray emission spectroscopy (XES), which has been proven to be a powerful bulk-sensitive probe of the moment in transition-metal compounds [7,8]. The local moment sensitivity of the *Kβ* CTC emission lines ($3p \rightarrow 1s$) originates from the large overlap between the 3*p* and 3*d*

orbitals. This gives the possibility to study locally the moment with a time scale of the order of femtoseconds [9] even in states without long-range magnetic order. Therefore it is the ideal tool to verify or disprove the predictions of the Mott-Hund scenario [1,5,10]. Complementary information is encoded in the unoccupied density of states around Fe which we have measured by means of *K* edge x-ray absorption spectroscopy (XAS).

At room temperature, the parent compound $BaFe_2As_2$ crystallizes in a tetragonal structure consisting of $(FeAs)^-$ iron arsenide layers separated by Ba^{2+} ions. We have studied two different families of hole-doped $BaFe_2As_2$ compounds: $Ba_{1-x}K_xFe_2As_2$ (out-of-plane doping) and $Ba(Fe_{1-x}Cr_x)_2As_2$ (in-plane doping). In $Ba_{1-x}K_xFe_2As_2$, partial substitution of Ba^{2+} with K^+ introduces holes in the $(FeAs)^-$ layers and superconductivity emerges [11–13]. In contrast, the $Ba(Fe_{1-x}Cr_x)_2As_2$ compounds, where Cr replaces iron atoms in the planes, are not superconducting [14,15]. K^+ injects one electron less than Ba^{2+} (the number of doped holes/Fe scales with $x_K/2$) while Cr^{2+} ($3d^4$) has two 3*d* electrons less than Fe^{2+} ($3d^6$) (the number of doped holes/Fe scales with $2x_{Cr}$). All samples were single crystals with the [001] direction as the surface normal, grown by the self-flux technique as detailed elsewhere [14,16,17]. Two sets of $Ba_{1-x}K_xFe_2As_2$ were measured covering the K-doping range $0 \leq x \leq 1$ (set 1 [16] with x = 0, 0.18, 0.6, 0.85, 1; and set 2 [17] with x = 0.08, 0.16, 0.25, 0.37) and one set of $Ba(Fe_{1-x}Cr_x)_2As_2$ with x = 0.026, 0.07, 0.12, 0.2, 0.3, 0.47. We also measured a single crystal of FeCrAs where Fe is non-magnetic [18–20].

II. EXPERIMENTAL DETAILS

The experiment was conducted at beamline ID26 of the European Synchrotron Radiation Facility (ESRF). Non-resonant Fe $K\beta$ XES measurements were recorded at incident energy 7200 eV. High-energy resolution fluorescence-detected x-ray absorption near edge structure (HERFD-XANES) spectra were obtained by setting the emission energy to the maximum of the $K\beta_{1,3}$ line while scanning the incoming energy through the absorption edge. The resulting spectrum is an approximation to the 1*s* photoabsorption cross section with sharper spectral features than in standard XAS [7,8]. Additional experimental details can be found in the appendix. All the measurements were performed at room temperature.

III. RESULTS

Fe *Kβ* CTC XES spectra were measured as a function of doping in $Ba_{1-x}K_xFe_2As_2$ ($0 \leq x \leq 1$) and $Ba(Fe_{1-x}Cr_x)_2As_2$ ($0.026 \leq x \leq 0.47$). Figure 1(a) shows the Fe *Kβ* CTC XES spectra for undoped $BaFe_2As_2$, the highest K- and Cr-content samples as representative examples, and the FeCrAs compound. As illustrated in Figure 1(a), the CTC *Kβ* emission lines arise from a $3p \rightarrow 1s$ decay after photoionization and, in the presence of a net 3*d* shell spin (*S*), two different groups of final states $K\beta_{1,3}$ and *Kβ*' are possible with opposite 3*p* core-hole spins and separated in energy by ΔE (within an LS-coupling scheme [9]). The spectral features are thus dominated by the 3*p*-3*d* exchange interaction and appear separated into the strong $K\beta_{1,3}$ peak and a broad *Kβ*' shoulder at lower emitted energy. Compared to FeCrAs, where a non-magnetic Fe is also in tetrahedral coordination with As [18–20], the spectra of $BaFe_2As_2$, KFe_2As_2 and $Ba(Fe_{0.53}Cr_{0.47})_2As_2$ show the $K\beta_{1,3}$ peak shifted to higher energies and a more intense *Kβ*' shoulder. This indicates that in the latter compounds the Fe atoms carry a higher net spin magnetic moment. In insulators a small intensity of the *Kβ*' feature is taken as an indication of a low-spin state and this spectral signature has been widely used to identify transitions from high- to low-spin as a function of pressure [21], temperature [22] or composition [23]. For metallic systems it has been observed that the *Kβ*' feature is very broad [24]. The splitting between the $K\beta_{1,3}$ and *Kβ*' is approximately given by $\Delta E = J(2S + 1)$ [25] where *J* is the exchange integral between the electrons in the 3*p* and 3*d* shells. It becomes visible in the difference spectra of Figure 1(a) and is about 10-15 eV in our compounds, which is compatible with a large 3*d* magnetic moment. The main change in the spectra upon doping is a shift of the $K\beta_{1,3}$ maximum to higher energies.

In order to quantify the evolution of the Fe local moment as a function of hole-doping from the CTC *Kβ* XES, we have applied the data reduction technique known as integrated absolute difference (IAD) [26]. This method allows obtaining the relative change in the local spin magnetic moment by integrating the absolute value of the difference between the spectrum of the sample and a reference spectrum. We chose $BaFe_2As_2$ as the reference and our IAD values thus represent the change in the local spin moment between each doped sample and the undoped compound. In Figure 1(a) are shown as example the difference spectra for the highest K- and Cr-content samples respectively and in Figure 1(b) the IAD values are plotted as a function of doped holes/Fe. In both cases a clear increase of the IAD value with hole-doping is observed, although

the amplitude of the enhancement is somewhat smaller for the K-doped samples. If the FeCrAs spectrum is used as reference for the IAD analysis as done in [27,28], the lineshape of the difference spectra for both the K- and Cr-doped compounds has the typical shape as reported in [27–31] showing a broad feature in the energy position of the *Kβ*' satellite and the downward-upward feature around the $K\beta_{1,3}$ peak. Interestingly, when using the parent compound $BaFe_2As_2$ as the reference instead, more structure is revealed. The K-doped compounds show a different modulation with an extra upward peak at the low energy side of the $K\beta_{1,3}$ maximum (about 7054 eV) while the Cr-doped compounds still follow the typical shape (see Fig. 1(a)). This may suggest a different mechanism for the increase in local moment possibly related to the in-plane (Cr^{2+}) and out-of-plane (K^+) doping (see also discussion of the HERFD-XANES data). However, at this point a detailed theoretical explanation for this observation eludes us.

Figure 2 shows the experimental HERFD-XANES spectra for the $Ba_{1-x}K_xFe_2As_2$ and $Ba(Fe_{1-x}Cr_x)_2As_2$ series. The spectrum of $BaFe_2As_2$ shows six distinct features denoted as *A*, *B*, *C*, *D*, *E* and *F* in the figure that are in agreement with previously reported conventional XANES spectra for the same compound [32,33]. All these features exhibit significant changes in the K-doped samples while upon Cr-doping the only significant variation is an intensity decrease in the *A* peak. The *A* peak intensity as a function of doped holes/Fe is shown in the inset of Figure 2. This feature just below the main rising edge occurs in the energy range of Fe 1*s* to 3*d* transitions. If inversion symmetry is absent as it is the case in the $FeAs_4$ tetrahedra, the metal 3*d* and 4*p* orbitals can mix resulting in strong $1s \rightarrow 4p$ dipolar transitions that dominate over the quadrupolar contribution at the same energy. The metal 4*p*-3*d* orbital mixing results in a large dipole contribution that originates from transitions to unoccupied metal *d* – ligand *p* hybrid bands [34]. Accordingly, previous works on related Fe based superconductors ascribed the *A* peak to the Fe-ligand orbital mixing [28–31,35,36]. In the appendix we include calculations of the HERFD-XANES spectra that nicely reproduce the experimental behaviour upon K- and Cr-doping. Our results suggest a significant enhancement of the Fe 3*d* – As 4*p* orbital mixing with K-doping and a modest decrease with Cr-doping. We investigated whether the behaviour of the *A* peak is correlated with the changes in the in-plane lattice parameter *a* of the tetragonal structure. In the inset of Figure 2 (right axis) we present the variation of the lattice parameter as a function of doped holes/Fe. The values for *a* were taken from diffraction experimental results [12,14]. Ba^{2+} substitution by K^+ out-of-plane induces shrinkage of the in-plane lattice

parameter along with a shortening of the Fe-As and Fe-Fe interatomic distances, whereas Fe^{2+} replacement by Cr^{2+} barely induces any structural change in the Fe-As plane. Clearly, the *A* peak intensity evolution is strongly correlated with the changes in the lattice parameter. In $Ba_{1-x}K_xFe_2As_2$, as a result of the shrinkage of the lattice parameter and with that of the interatomic distances, the Fe 3*d* – As 4*p* orbital mixing increases as reflected in the rise of the *A* peak intensity. Compared to K-doping, Cr-doping hardly affects the lattice parameter except for a subtle increment that can account for a small decrease of the orbital mixing and in turn of the *A* peak intensity. We include in the appendix the Fe *Kβ* valence-to-core (VTC) XES measurements that also indicate changes in the occupied density of states correlated with the evolution of the lattice parameter and the variations in covalency.

IV. DISCUSSION AND CONCLUSIONS

A finite IAD value is generally attributed to a change in the 3*p* – 3*d* exchange interaction as it reflects a modification of the *Kβ*'-$K\beta_{1,3}$ splitting ΔE. We recall that ΔE depends on the 3*p* – 3*d* exchange integral *J* and the valence shell spin *S* [25]. Stronger metal-ligand covalency may be interpreted in terms of a larger radial distribution of the effective (Wannier) metal *d*-orbitals used in the description of the electron density, implying a decrease of *J*. The influence of the metal – ligand covalency on the *Kβ* CTC spectra has been reported earlier in different works [7,37,38]. While *J* can be assumed to vary very little with Cr-doping, it decreases along the $Ba_{1-x}K_xFe_2As_2$ series with increasing K-content as a result of the spread of the Wannier orbitals of Fe 3*d* character. Thus, the changes in the *Kβ* emission due to an increase in *S* caused by the hole-doping are counteracted by a decrease in *J* arising from the spread of the Wannier orbitals. This picture may explain the two types of lineshape in the *Kβ* difference spectra (cf. Figure 1(a)) and the smaller increase in IAD in the K-doping as compared to the Cr-doping series. The intensity of the *A* peak (I_A) in the HERFD-XANES spectra reflects the amount of 3*d*-4*p* mixing and implicitly the variations in the 3*p* – 3*d* exchange integral. Rescaling of the IAD values by a factor $I_{A(x)}/I_{A(x=0)}$ along both series will thus reduce the influence of a variation of *J* and allow comparison of the modification arising from a change of *S* only. The rescaled IAD values are shown in Figure 3. The two types of hole-doping follow the same clear trend, in agreement with the theoretical scenario we discussed, which predicts that correlations increase as we approach a Hund-promoted Mott insulator at half-filling [1,5,18]. A more direct comparison can be drawn

by computing the local magnetic moment within Density Functional Theory (DFT) combined with Slave-spin mean-field (see appendix for details on the method). The theoretical spin-spin local correlation function $<S_zS_z>$, which increases monotonically with the total local magnetic moment (e.g. at low U, $S(S+1) = 3<SzSz>$) is reported in the inset of Fig. 3 as a function of interaction strength U. It is clear that in the uncorrelated ($U = 0$) limit (as described by DFT) the change in local magnetic moment between the compounds is negligible. In contrast, at large U, where the system is a Mott insulator at half-filling, a different behaviour is found, with the moment increasing towards saturated values as half-filling is approached by hole-doping. Consequently, the saturation value at large U for KFe_2As_2 is larger than for $BaFe_2As_2$. This effect is due to the hole-doping, while the change in the lattice structure between the two compounds acts in the opposite direction. This is visible as a slightly smaller value of the magnetic moment for KFe_2As_2 at small to intermediate U, caused by a small increase in the DFT bare bandwidth of the latter, compared to $BaFe_2As_2$, which embodies the increased covalency. The doping effect is however dominant at larger U. The absence of this covalency effect due to the lack of structural changes in the Cr-doped samples thus favours the slightly larger increase of the moment compared to the K-doped case corroborating the trend we observe in the measurements.

These results appear in sharp contrast with the conclusions of inelastic neutron scattering (INS) on the K-doped samples which extract an opposite trend from the low-energy magnetic response, the moment decreases with hole-doping and appears to vanish in KFe_2As_2 [39]. Although INS is fast with respect to standard magnetic probes, it is actually not as fast as XES-XAS. Such a difference can therefore result in the underestimation of the instantaneous magnetic moment, as already demonstrated in the 122 family [40]. However, in the present case, the results of these two experimental probes are opposite, the origin of which needs to be understood. In INS the magnetic moment is obtained by integrating over frequency the dynamical magnetic response, and is therefore highly sensitive on the actual cutoff energy. To capture the important contributions at a frequency larger than 100 meV, a fast probe such as XES is necessary [41]. Thus we could reconcile the present results with INS assuming that in KFe_2As_2, where the low-energy (below 100 meV) signal almost vanishes [39], there is instead an important weight at larger frequencies beyond the cutoff used in [39], while in $BaFe_2As_2$ a larger fraction of the moment lives at low frequency. This substantial difference between the two

compounds can be a consequence of the different degree of correlation and low-temperature magnetic properties of the two systems. The lack of a magnetic ordering in KFe_2As_2 can enhance the dynamical nature of the magnetic moment with respect to compounds which, at lower temperatures, develop a static magnetic moment.

The XES-XAS study presented in this Letter clearly shows an increase of the Fe instantaneous local moment upon hole-doping in $BaFe_2As_2$, providing experimental evidence of the Hund-Mott physics model [1,5,10] which is an important input for the community studying Fe-based superconductors. By combining results from x-ray emission with x-ray absorption spectroscopy, we have been able to disentangle the different influence of structural and correlation effects on the local spin moment in K- and Cr-doped $BaFe_2As_2$ clearly confirming that the doping-induced correlation effects are the driving force behind the development of the local moments.

ACKNOWLEDGEMENTS

The authors thank ESRF for granting beam time and ID26 beamline staff for their assistance during the experiments. This research was supported in part by the National Science Foundation under Grant No. NSF PHY11-25915, through the support of LdM and YJK for the participation to the KITP IRONICS14 workshop. LdM would also like to thank discussions with M. Casula and K. Gilmore, M.B. Lepetit. GG and MC acknowledge funding by FP7/ERC Grant ``SUPERBAD" (GA 240524) and SISSA/CNR project “Superconductivity, Ferroelectricity and Magnetism in bad metals”. YJK acknowledges the support from Natural Science and Engineering Research Council of Canada. The work at ORNL was supported by the U.S. Department of Energy (DOE), Office of Science, Basic Energy Sciences (BES) Materials Sciences and Engineering Division.

Note added.— An increase in the Fe local moment with hole-doping has recently also been observed by Pelliciari and collaborators in $Ba_{1-x}K_xFe_2As_2$ (x = 0, 0.25, 0.4, 0.6) [42].

APPENDIX

In this section we provide additional information about the experimental details, results of Fe *Kβ* valence-to-core (VTC) XES measurements, simulations of the HERFD-XANES spectra across the Fe *K* edge and details about slave-spin mean-field calculations of the local moment.

1. Additional experimental details

A schematic of the measurement configuration is provided in Figure 4. The incoming radiation from the undulators fundamental was monochromatized by a pair of cryogenically cooled Si(111) crystals. A reference Fe metallic foil was used to calibrate the monochromator energy by setting the first inflection point of the Fe *K* edge at 7112 eV. The x-ray beam is naturally linearly polarized in the plane. The surface of the plate-like single crystal samples was aligned to 45º with respect to the incident beam direction. This configuration provides results close to measurements on a polycrystal sample case as the electric field vector (**E**) of the x-rays and the sample [001] direction are at 45º which means that the *ab* plane and [001] direction are probed equally. The penetration depth at the Fe *K* edge is of the order of a few μm and thus all our data are representative of the bulk and unaffected by the sample surface quality.

The emission spectrometer employed five spherically bent Ge(620) analyzer crystals that were arranged with the sample and avalanche photodiode (APD) detector in a vertical Rowland geometry (R = 1 m). The horizontal scattering angle was set to 90° with respect to the central analyzer crystal to minimize the background due to scattering. The total experimental broadening, determined as full width at half maximum of the elastic profiles, was 1.3 eV.

Both Fe *Kβ* CTC XES and HERFD-XANES spectra were normalized in area using the ranges 7025-7080 eV and 7105-7190 eV respectively. A minimum of two Fe *Kβ* CTC XES spectra were measured per sample and the corresponding zero signal in each case (i.*e.* the difference spectra between two equivalent measurements) was checked to assess the experimental error.

2. Fe K*β* VTC XES spectra

To complete the *Kβ* XES study, we measured the VTC emission lines, also referred to as *Kβ* satellite lines. While the CTC *Kβ* lines are sensitive to the local spin magnetic moment, VTC emission lines mainly probe the occupied metal *p*-density of states (DOS) up to 25 eV below the Fermi energy which is strongly mixed with ligand *s* and *p* orbitals [43]. These emission lines

correspond to transitions from valence orbitals with metal *p* character and the spectrum can be divided into the $K\beta_{2,5}$ (main peak) and $K\beta''$ (feature at lower emission energies) regions. Figures 5(a) and 5(b) show the VTC $K\beta$ spectra separately for the $Ba_{1-x}K_xFe_2As_2$ and $Ba(Fe_{1-x}Cr_x)_2As_2$ series after background removal. The VTC spectra were further treated by performing a background subtraction in order to remove the contribution from the CTC main line tail. For that, the background was modelled using several Voigt functions that were fitted to the data points above (7120-7130 eV) and below (7060-7085 eV) the VTC features following the procedure described in [43].

Upon K-doping the intensity of the features decreases until x = 0.6, from where a recovery in the intensity is observed coupled with a shift towards higher energies. The intensity decreases as well upon Cr-doping but no major shift is observed. The full VTC spectra were fitted using four Lorentzian functions to analyze the $K\beta_{2,5}$ and $K\beta''$ peaks. The evolution of the $K\beta_{2,5}$ peak center position in energy is shown in Figure 5(c) as a function of doped holes/Fe. A similar trend is observed for the $K\beta''$ peak center (not plotted). We have included in the same figure the evolution of the in-plane lattice parameter *a* taken from diffraction data reported in refs. [12] and [14] for $Ba_{1-x}K_xFe_2As_2$ and $Ba(Fe_{1-x}Cr_x)_2As_2$ respectively. While little variation is observed with Cr-doping, the lattice parameter shrinks upon K-doping with a consequent shortening of the Fe-As and Fe-Fe distances. We observe a shift to higher energies of the $K\beta_{2,5}$ line with increasing K-content (about 0.5 eV shift between x = 0 and x = 1). This means that shorter bond lengths increase the Fe-ligand orbital mixing and push the occupied *p*-DOS to higher energies. Conversely, Fe^{2+} substitution by Cr^{2+} directly in-plane barely affects the lattice constant compared with K-doping. Accordingly, the $K\beta_{2,5}$ line does not shift notably with Cr-doping.

3. Simulations of the HERFD-XANES spectra across the Fe *K* edge

With the aim of gaining more insight into the origin of the different spectral features and their evolution with doping we performed simulations in the framework of the multiple scattering (MS) theory using the FDMNES code [44]. That is, density functional theory calculations in the local density approximation (DFT-LDA) and one-electron transitions. The tetragonal crystal structures (space group *I4/mmm*) of $BaFe_2As_2$ [45] and KFe_2As_2 [12] were used as input in the simulations, carried out in real space with a muffin-tin approximation for the potential. For the exchange–correlation part, the real Hedin, Lundqvist and Von Barth potential

was used. The spectra were convoluted using an appropiate Lorentzian function. To compare with the experiment, the computed energy values in the calculations were aligned with the experimental energy scale with the same rigid shift so that the first peak coincides for the KFe_2As_2 compound. The cluster size around the central absorber Fe atom that is considered in the calculations is progressively increased in order to monitor the effect of each neighbouring atom shell on the spectral features.

Figure 6(a) shows the calculated spectra for $BaFe_2As_2$ and KFe_2As_2 obtained for a cluster radius of 6.6 Å (about 50 atoms) which corresponds to the size beyond which only minor spectral changes are observed. A third calculation is included in which the atomic positions given by the $BaFe_2As_2$ structure were used but with 50% of the Fe atoms randomly replaced by Cr in order to mimic the x = 0.47 Cr-doping effect. The calculations nicely reproduce the experimental spectral line shape. The *A* peak appears in the calculations when the four As nearest neighbours conforming the $FeAs_4$ tetrahedra (at 2.40 Å and 2.38 Å for the $BaFe_2As_2$ and KFe_2As_2 structures respectively) are included in the cluster, corroborating that it arises from the mixing between the Fe 3*d* and As 4*p* orbitals. Substitution of Fe by Cr slightly reduces this 3*d*-4*p* orbital mixing as illustrated in the simulation for Fe/Cr in 1:1 proportion, where a weaker *A* peak is observed in accordance with the experimental data. Moreover, the *A* peak was found to be of predominantly dipolar character since when adding quadrupolar transitions in the calculations only a tiny intensity increase (lower than 5 %) was obtained. For KFe_2As_2, the *B* feature appears when the first four K neighbours at 3.94 Å are included. Similarly, for $BaFe_2As_2$ the *C* feature is seen once the first four Ba neighbours at 3.81 Å are considered. The *D* - *F* spectral features at higher incident energy result from contributions of neighbouring atoms beyond the first coordination shells and markedly differ between $BaFe_2As_2$ and KFe_2As_2.

Finally, in order to check the K-doping effect in the simulations, Ba(K) atoms were randomly replaced by K(Ba) in the cluster for 50 and 100% substitution rates while maintaining the crystal structure of $BaFe_2As_2$(KFe_2As_2). As shown in Figures 6(b) and 6(c), we find that these calculations reproduce the main changes in the experimental spectra upon K-doping. This result indicates that, in addition to the structural changes, the presence of a particular electronic configuration in the tetragonal structure is also responsible for the enhanced Fe 3*d*-As 4*p* orbital mixing.

4. Slave-spin mean-field theoretical calculations

Material-specific many-body calculations of the local moment as a function of the electron-interaction strength reported in the inset of Fig. 3 are performed using Density Functional Theory with the Generalized Gradient Approximation for the exchange-correlation potential according to the Perdew-Burke-Ernzerhof recipe as implemented in Quantum Espresso [46]. The Wannier90 code [47] is used to find the basis of maximally localized Wannier orbitals (10 orbitals, 5 orbitals/Fe) describing the conduction bands. The tight-binding Hamiltonian for the conduction electrons in this basis is supplemented by an explicit local interaction term *à la Hubbard* reading:

$$H_{int} = U\sum_{i,m} n^d_{im\uparrow} n^d_{im\downarrow} + (U-2J)\sum_{i,m>m',\sigma} n^d_{im\sigma} n^d_{im'\bar{\sigma}} + (U-3J)\sum_{i,m>m',\sigma} n^d_{im\sigma} n^d_{im\sigma} \quad \text{(A1)}$$

where $n^d_{im\sigma}$ is the number operator for electrons in orbital m of site i with spin σ, and $\bar{\sigma}$ is the opposite of σ. This multi-orbital Hubbard model is solved within slave-spin mean-field theory [48,49] (see supplemental material of Ref. [1] for further details).

The quantity reported in Fig. 3, $< S_z S_z >$, is the equal-time correlation function between the z-component of the total spin on the Wannier orbitals. This is easily related the total spin "on site" in the uncorrelated limit, since

$$< S^2 > = < S_x S_x > + < S_y S_y > + < S_z S_z > = 3 < S_z S_z > \quad \text{(A2)}$$

because of rotational invariance.

The interaction term in the density-density approximation used here breaks this rotational invariance so that the previous equality does not hold at finite *U*. There, it is easy to understand that a larger component of the correlation function is found in the z direction, thanks to the fact that the interaction couples the spins in this direction. Nevertheless the correlation function remains a monotonous function of *S*, and a saturated value of the correlation function represents a saturated value of the total local spin to its maximum value.

REFERENCES

[1] L. de' Medici, G. Giovannetti, and M. Capone, Phys. Rev. Lett. **112**, 177001 (2014).

[2] P. O. Sprau, A. Kostin, A. Kreisel, A. E. Böhmer, V. Taufour, P. C. Canfield, S. Mukherjee, P. J. Hirschfeld, B. M. Andersen, and J. C. S. Davis, arXiv:1611.02134v1 (2016).

[3] A. Kreisel, B. M. Andersen, P. O. Sprau, A. Kostin, J. C. S. Davis, and P. J. Hirschfeld, arXiv:1611.02643v1 (2016).

[4] F. Hardy, A. E. Böhmer, L. De'Medici, M. Capone, G. Giovannetti, R. Eder, L. Wang, M. He, T. Wolf, P. Schweiss, R. Heid, A. Herbig, P. Adelmann, R. A. Fisher, and C. Meingast, Phys. Rev. B **94**, 205113 (2016).

[5] T. Misawa, K. Nakamura, and M. Imada, Phys. Rev. Lett. **108**, 177007 (2012).

[6] L. de' Medici, in *Iron-Based Supercond.*, edited by P. D. Johnson, G. Xu, and W.-G. Yin (Springer International Publishing, Switzerland, 2015), pp. 409–441.

[7] P. Glatzel and U. Bergmann, Coord. Chem. Rev. **249**, 65 (2005).

[8] M. Rovezzi and P. Glatzel, Semicond. Sci. Technol. **29**, 23002 (2014).

[9] M. Taguchi, T. Uozumi, and A. Kotani, J. Phys. Soc. Japan **66**, 247 (1997).

[10] H. Ishida and A. Liebsch, Phys. Rev. B **81**, 54513 (2010).

[11] M. Rotter, M. Tegel, and D. Johrendt, Phys. Rev. Lett. **101**, 107006 (2008).

[12] S. Avci, O. Chmaissem, D. Y. Chung, S. Rosenkranz, E. A. Goremychkin, J. P. Castellan, I. S. Todorov, J. A. Schlueter, H. Claus, A. Daoud-Aladine, D. D. Khalyavin, M. G. Kanatzidis, and R. Osborn, Phys. Rev. B **85**, 184507 (2012).

[13] H. Chen, Y. Ren, Y. Qiu, W. Bao, R. H. Liu, G. Wu, T. Wu, Y. L. Xie, X. F. Wang, Q. Huang, and X. H. Chen, Europhys. Lett. **85**, 17006 (2009).

[14] A. S. Sefat, D. J. Singh, L. H. VanBebber, Y. Mozharivskyj, M. A. McGuire, R. Jin, B. C. Sales, V. Keppens, and D. Mandrus, Phys. Rev. B **79**, 224524 (2009).

[15] K. Marty, A. D. Christianson, C. H. Wang, M. Matsuda, H. Cao, L. H. Vanbebber, J. L. Zarestky, D. J. Singh, A. S. Sefat, and M. D. Lumsden, Phys. Rev. B **83**, 60509 (2011).

[16] A. E. Böhmer, F. Hardy, L. Wang, T. Wolf, P. Schweiss, and C. Meingast, Nat. Commun. **6**, 7911 (2015).

[17] H. Luo, Z. Wang, H. Yang, P. Cheng, X. Zhu, and H.-H. Wen, Supercond. Sci. Technol. **21**, 125014 (2008).

[18] S. Ishida, T. Takiguchi, S. Fujii, and S. Asano, Phys. B Condens. Matter **217**, 87 (1996).

[19] W. Wu, A. McCollam, I. Swainson, P. M. C. Rourke, D. G. Rancourt, and S. R. Julian, Europhys. Lett. **85**, 17009 (2009).

[20] J. G. Rau and H.-Y. Kee, Phys. Rev. B **84**, 104448 (2011).

[21] J.-P. Rueff, C. Kao, V. Struzhkin, J. Badro, J. Shu, R. J. Hemley, and H. Mao, Phys. Rev. Lett. **82**, 4 (1998).

[22] G. Vankó, J.-P. Rueff, A. Mattila, Z. Németh, and A. Shukla, Phys. Rev. B **73**, 24424

(2006).

[23] M. Sikora, K. Knizek, C. Kapusta, and P. Glatzel, J. Appl. Phys. **103**, 07C907 (2008).

[24] G. Hölzer, M. Fritsch, M. Deutsch, J. Härtwig, and E. Förster, Phys. Rev. A **56**, 4554 (1997).

[25] K. Tsutsumi, H. Nakamori, and K. Ichikawa, Phys. Rev. B **13**, 929 (1976).

[26] G. Vankó, T. Neisius, G. Molnar, F. Renz, S. Karpati, A. Shukla, and F. M. F. de Groot, J. Phys. Chem. B **110**, 11647 (2006).

[27] H. Gretarsson, A. Lupascu, J. Kim, D. Casa, T. Gog, W. Wu, S. R. Julian, Z. J. Xu, J. S. Wen, G. D. Gu, R. H. Yuan, Z. G. Chen, N.-L. Wang, S. Khim, K. H. Kim, M. Ishikado, I. Jarrige, S. Shamoto, J.-H. Chu, I. R. Fisher, and Y.-J. Kim, Phys. Rev. B **84**, 100509 (2011).

[28] H. Gretarsson, S. R. Saha, T. Drye, J. Paglione, J. Kim, D. Casa, T. Gog, W. Wu, S. R. Julian, and Y.-J. Kim, Phys. Rev. Lett. **110**, 47003 (2013).

[29] J. M. Chen, S. C. Haw, J. M. Lee, T. L. Chou, S. A. Chen, K. T. Lu, Y. C. Liang, Y. C. Lee, N. Hiraoka, H. Ishii, K. D. Tsuei, E. Huang, and T. J. Yang, Phys. Rev. B **84**, 125117 (2011).

[30] L. Simonelli, N. L. Saini, Y. Mizuguchi, Y. Takano, T. Mizokawa, G. Baldi, and G. Monaco, J. Phys. Condens. Matter **24**, 415501 (2012).

[31] Y. Yamamoto, H. Yamaoka, M. Tanaka, H. Okazaki, T. Ozaki, Y. Takano, J.-F. Lin, H. Fujita, T. Kagayama, K. Shimizu, N. Hiraoka, H. Ishii, Y.-F. Liao, K.-D. Tsuei, and J. Mizuki, Sci. Rep. **6**, 30946 (2016).

[32] J. Cheng, W. S. Chu, G. Wu, H. F. Zhao, W. Xu, J. Zhou, L. J. Zhang, X. H. Chen, and Z. Y. Wu, J. Synchrotron Radiat. **17**, 730 (2010).

[33] E. M. Bittar, C. Adriano, T. M. Garitezi, P. F. S. Rosa, L. Mendonça-Ferreira, F. Garcia, G. de M. Azevedo, P. G. Pagliuso, and E. Granado, Phys. Rev. Lett. **107**, 267402 (2011).

[34] F. de Groot, G. Vankó, and P. Glatzel, J. Phys. Condens. Matter **21**, 104207 (2009).

[35] B. C. Chang, Y. B. You, T. J. Shiu, M. F. Tai, H. C. Ku, Y. Y. Hsu, L. Y. Jang, J. F. Lee, Z. Wei, K. Q. Ruan, and X. G. Li, Phys. Rev. B **80**, 165108 (2009).

[36] B. Joseph, A. Iadecola, L. Simonelli, Y. Mizuguchi, Y. Takano, T. Mizokawa, and N. L. Saini, J. Phys. Condens. Matter **22**, 485702 (2010).

[37] J. P. Rueff and A. Shukla, Rev. Mod. Phys. **82**, 847 (2010).

[38] C. J. Pollock, M. U. Delgado-Jaime, M. Atanasov, F. Neese, and S. DeBeer, J. Am. Chem. Soc. **136**, 9453 (2014).

[39] M. Wang, C. Zhang, X. Lu, G. Tan, H. Luo, Y. Song, M. Wang, X. Zhang, E. A. Goremychkin, T. G. Perring, T. A. Maier, Z. Yin, K. Haule, G. Kotliar, and P. Dai, Nat. Commun. **4**, 2874 (2013).

[40] N. Mannella, J. Phys. Condens. Matter **26**, 473202 (2014).

[41] A. Toschi, R. Arita, P. Hansmann, G. Sangiovanni, and K. Held, Phys. Rev. B **86**, 64411 (2012).

[42] J. Pelliciari, Y. Huang, K. Ishii, C. Zhang, P. Dai, G. F. Chen, L. Xing, X. Wang, C. Jin, H. Ding, P. Werner, and T. Schmitt, arXiv:1607.04038v1 (2016).

[43] E. Gallo and P. Glatzel, Adv. Mater. **26**, 7730 (2014).

[44] Y. Joly, Phys. Rev. B **63**, 125120 (2001).

[45] N. Eguchi, M. Kodama, F. Ishikawa, A. Nakayama, A. Ohmura, Y. Yamada, and S. Nakano, J. Phys. Conf. Ser. **400**, 22017 (2012).

[46] P. Giannozzi, S. Baroni, N. Bonini, M. Calandra, R. Car, C. Cavazzoni, D. Ceresoli, G. L. Chiarotti, M. Cococcioni, I. Dabo, A. Dal Corso, S. de Gironcoli, S. Fabris, G. Fratesi, R. Gebauer, U. Gerstmann, C. Gougoussis, A. Kokalj, M. Lazzeri, L. Martin-Samos, N. Marzari, F. Mauri, R. Mazzarello, S. Paolini, A. Pasquarello, L. Paulatto, C. Sbraccia, S. Scandolo, G. Sclauzero, A. P. Seitsonen, A. Smogunov, P. Umari, and R. M. Wentzcovitch, J. Phys. Condens. Matter **21**, 395502 (2009).

[47] A. A. Mostofi, J. R. Yates, Y. S. Lee, I. Souza, D. Vanderbilt, and N. Marzari, Comput. Phys. Commun. **178**, 685 (2008).

[48] L. De'Medici, A. Georges, and S. Biermann, Phys. Rev. B **72**, 205124 (2005).

[49] S. R. Hassan and L. DeMedici, Phys. Rev. B **81**, 35106 (2010).

FIGURE CAPTIONS

Figure 1. (a) Normalized Fe *Kβ* CTC XES spectra of $BaFe_2As_2$, KFe_2As_2, $Ba(Fe_{0.53}Cr_{0.47})_2As_2$ and FeCrAs at room temperature together with the difference spectra between $BaFe_2As_2$ and the KFe_2As_2 (blue) and $Ba(Fe_{0.53}Cr_{0.47})_2As_2$ (green) compounds respectively. Inset: simplified one-electron scheme for the *Kβ* CTC XES process where filled and empty circles represent electrons and holes. (b) IAD values derived from the Fe *Kβ* CTC XES spectra of the $Ba_{1-x}K_xFe_2As_2$ and $Ba(Fe_{1-x}Cr_x)_2As_2$ series normalized to the spectral area, shown as a function of doped holes/Fe ($x_K/2$ and $2x_{Cr}$ for K- and Cr-doping series respectively). Circles and triangles differentiate the K-doped samples from sets 1 and 2 respectively. The error bars are as estimated from comparison of equivalent measurements taken in the same conditions either during a different experimental session or in a sample from a different batch.

Figure 2. Normalized HERFD-XANES spectra at the Fe *K* edge of $Ba_{1-x}K_xFe_2As_2$ ($0 \leq x \leq 1$) and $Ba(Fe_{1-x}Cr_x)_2As_2$ ($0.026 \leq x \leq 0.47$) series at room temperature. Inset: Evolution of *A* peak intensity (symbols; left axis) as a function of doped holes/Fe ($x_K/2$ and $2x_{Cr}$ for K- and Cr-doping series respectively). Circles and triangles differentiate the K-doped samples from sets 1 and 2

respectively. On the right axis the data of the tetragonal lattice parameter *a* from refs. [12] and [14] is plotted for a direct comparison.

Figure 3. Rescaled IAD values taking into account the changes in the *A* peak intensity derived from the HERFD-XANES data. Inset: DFT+Slave-spin mean-field calculations of the local magnetic moment for $BaFe_2As_2$ (Fe in d^6 configuration) and KFe_2As_2 (Fe in $d^{5.5}$ configuration) as a function of the interaction strength *U*, for Hund's coupling J/U=0.25 [1]. A strong increase of the local moment with hole-doping is only observed in the region (U>2.5eV) influenced by the Mott insulating phase realized for a half-filled configuration d^5. For further details see the appendix section.

Figure 4. Schematic (top view) of the measurement configuration as described in the experimental details section.

Figure 5. Normalized Fe *Kβ* VTC XES spectra of (a) $Ba_{1-x}K_xFe_2As_2$ ($0 \leq x \leq 1$) and (b) $Ba(Fe_{1-x}Cr_x)_2As_2$ ($0.026 \leq x \leq 0.47$) series after background removal. (c) Evolution of $K\beta_{2,5}$ peak center position in energy (symbols; left axis) as a function of doped holes/Fe. Circles and triangles differentiate the K-doped samples from sets 1 and 2 respectively. On the right axis the data of the tetragonal lattice parameter *a* from refs. [12] and [14] is plotted for a direct comparison and they are shown with lines plus symbols.

Figure 6. (a) Calculated XANES spectra for a cluster size of 6.6 Å around Fe (about 50 atoms) using the tetragonal crystal structures of $BaFe_2As_2$ and KFe_2As_2. To simulate the effects of Cr-doping Fe atoms were randomly replaced by Cr for 50 % substitution rate while keeping the atomic positions of the $BaFe_2As_2$ structure. (b) and (c) panels show the effect of replacing Ba and K atoms in the clusters while maintaining the atomic positions of the $BaFe_2As_2$ and KFe_2As_2 crystal structures respectively for 50 and 100 % substitution rates.

Figure 1.

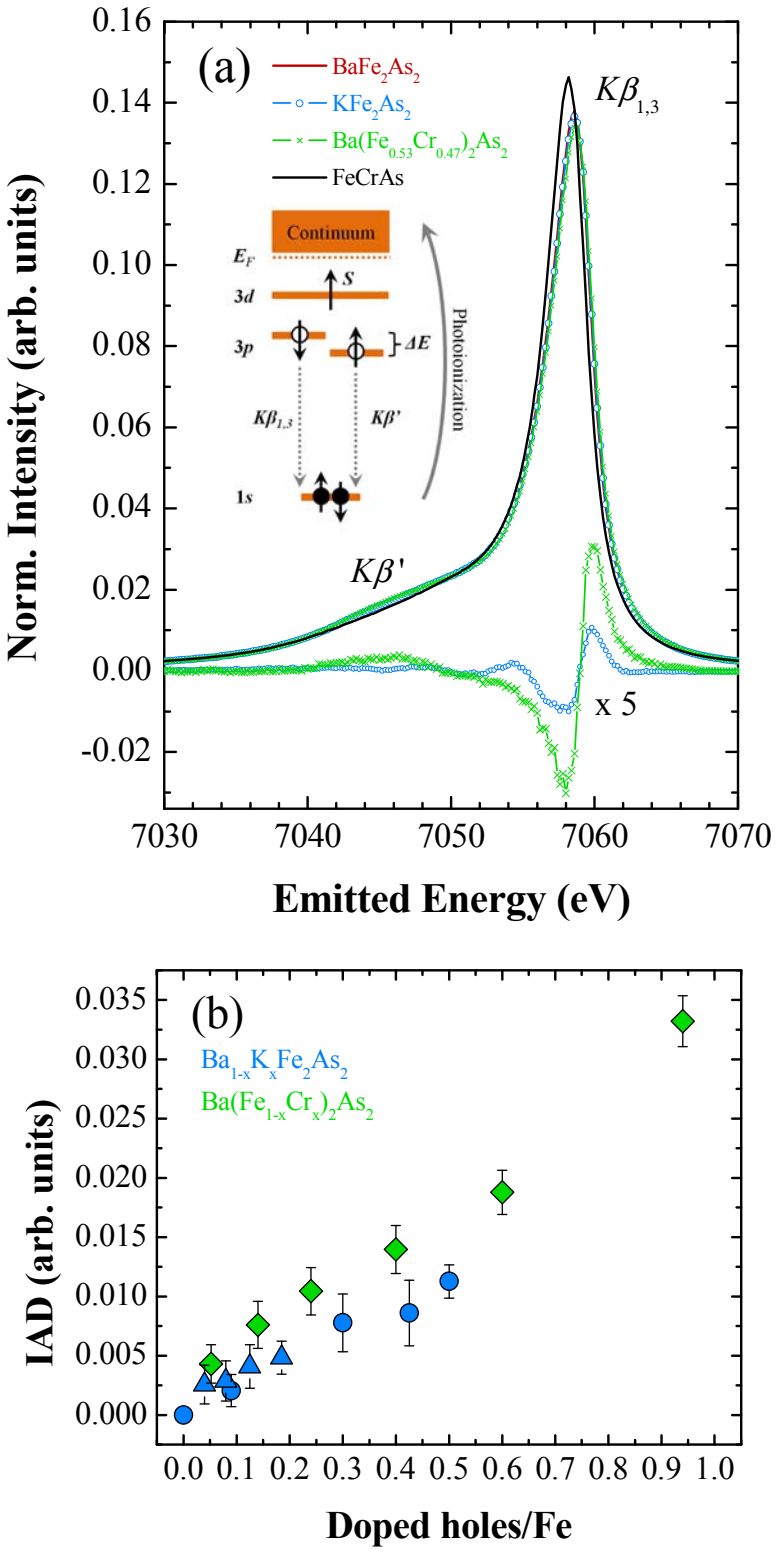
(a)
BaFe2As2
KFe2As2
Ba(Fe0.53Cr0.47)2As2
FeCrAs
Continuum
EF
3d
3p
1s
S
ΔE
Kβ1,3
Kβ'
Photoionization
Kβ1,3
Kβ'
x 5
Norm. Intensity (arb. units)
Emitted Energy (eV)
0.16
0.14
0.12
0.10
0.08
0.06
0.04
0.02
0.00
-0.02
7030
7040
7050
7060
7070
(b)
Ba1-xKxFe2As2
Ba(Fe1-xCrx)2As2
IAD (arb. units)
Doped holes/Fe
0.035
0.030
0.025
0.020
0.015
0.010
0.005
0.000
0.0 0.1 0.2 0.3 0.4 0.5 0.6 0.7 0.8 0.9 1.0

Figure 2.

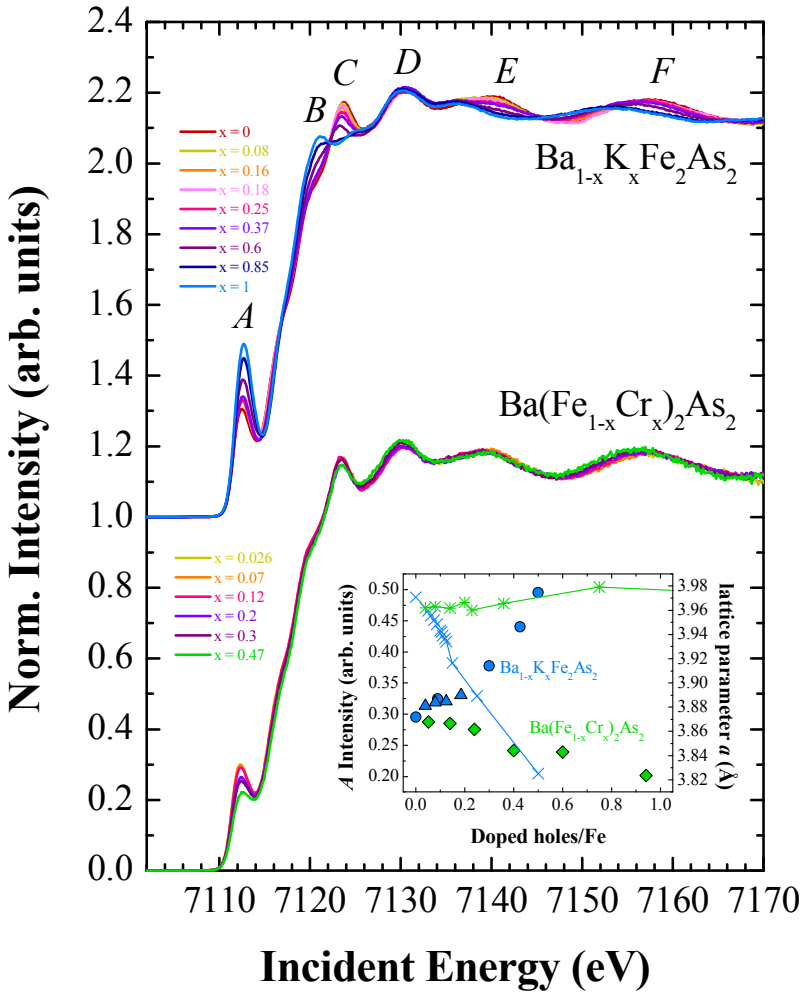
Norm. Intensity (arb. units)
Incident Energy (eV)
A
B
C
D
E
F
x = 0
x = 0.08
x = 0.16
x = 0.18
x = 0.25
x = 0.37
x = 0.6
x = 0.85
x = 1
Ba1-xKxFe2As2
x = 0.026
x = 0.07
x = 0.12
x = 0.2
x = 0.3
x = 0.47
Ba(Fe1-xCrx)2As2
A Intensity (arb. units)
lattice parameter a (Å)
Doped holes/Fe

Figure 3.

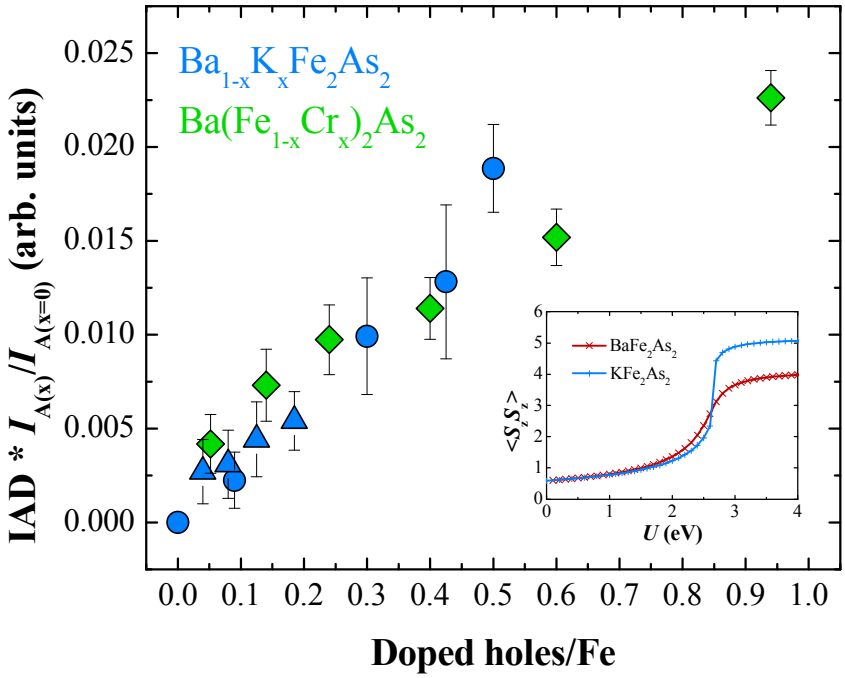
Ba1-xKxFe2As2
Ba(Fe1-xCrx)2As2
IAD * IA(x)/IA(x=0) (arb. units)
Doped holes/Fe
0.000
0.005
0.010
0.015
0.020
0.025
0.0
0.1
0.2
0.3
0.4
0.5
0.6
0.7
0.8
0.9
1.0
BaFe2As2
KFe2As2
<SzSz>
U (eV)
0
1
2
3
4
5
6

Figure 4.

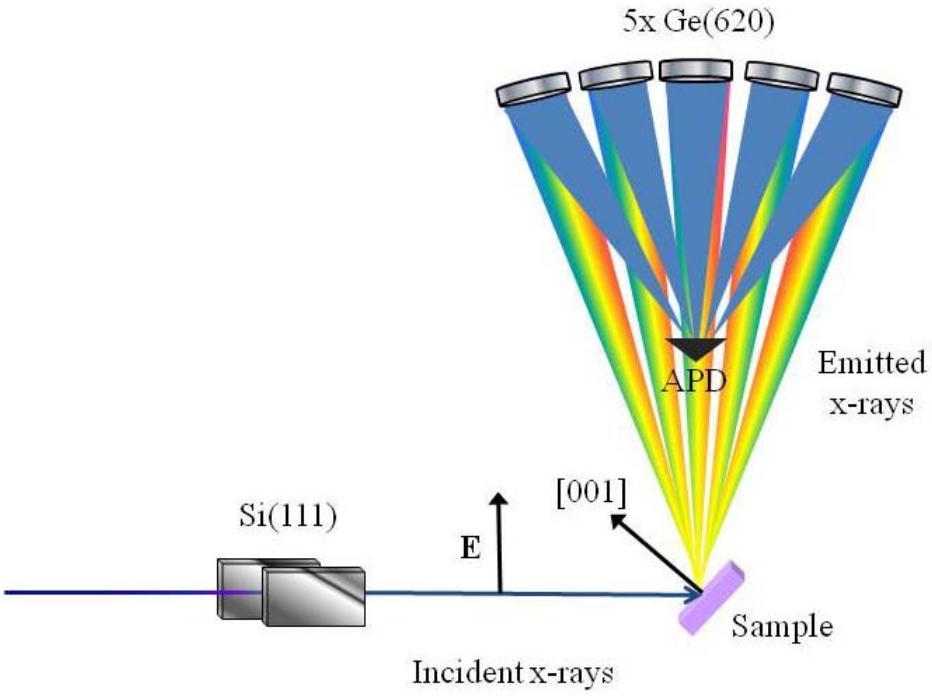
5x Ge(620)
APD
Emitted
x-rays
[001]
E
Si(111)
Sample
Incident x-rays

Figure 5.

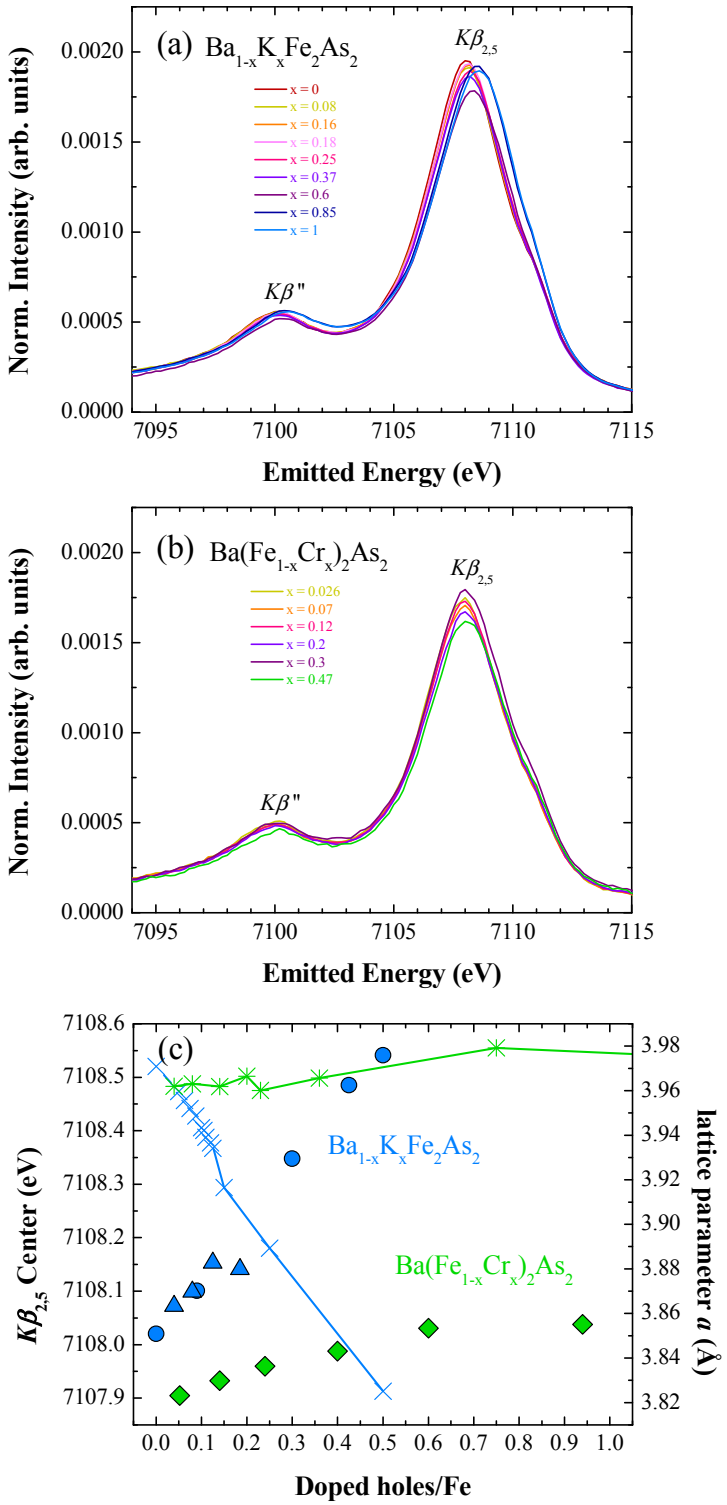
(a) Ba1-xKxFe2As2
x = 0
x = 0.08
x = 0.16
x = 0.18
x = 0.25
x = 0.37
x = 0.6
x = 0.85
x = 1
Kβ2,5
Kβ"
Norm. Intensity (arb. units)
Emitted Energy (eV)
(b) Ba(Fe1-xCrx)2As2
x = 0.026
x = 0.07
x = 0.12
x = 0.2
x = 0.3
x = 0.47
Kβ2,5
Kβ"
Norm. Intensity (arb. units)
Emitted Energy (eV)
(c)
Ba1-xKxFe2As2
Ba(Fe1-xCrx)2As2
Kβ2,5 Center (eV)
lattice parameter a (Å)
Doped holes/Fe

Figure 6.

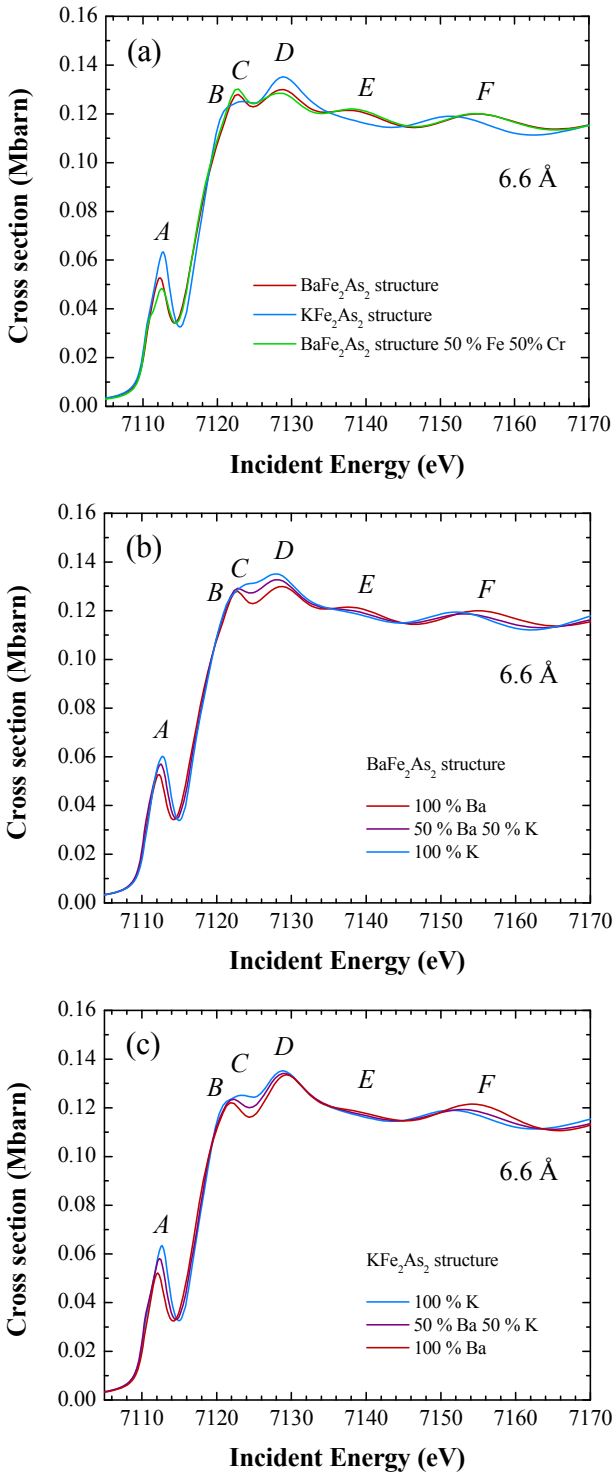
(a)
A
B
C
D
E
F
6.6 Å
BaFe2As2 structure
KFe2As2 structure
BaFe2As2 structure 50 % Fe 50% Cr
(b)
6.6 Å
BaFe2As2 structure
100 % Ba
50 % Ba 50 % K
100 % K
(c)
6.6 Å
KFe2As2 structure
100 % K
50 % Ba 50 % K
100 % Ba
Cross section (Mbarn)
Incident Energy (eV)
0.00
0.02
0.04
0.06
0.08
0.10
0.12
0.14
0.16
7110
7120
7130
7140
7150
7160
7170